JACS
JOURNAL OF THE AMERICAN CHEMICAL SOCIETY
Article

# $Fe_{3-x}Ti_xO_4$ Nanoparticles as Tunable Probes of Microbial Metal Oxidation

Juan Liu,*[,†] Carolyn I. Pearce,[†] Chongxuan Liu,[†] Zheming Wang,[†] Liang Shi,[†] Elke Arenholz,[‡] and Kevin M. Rosso[†]

[†]Pacific Northwest National Laboratory, Richland, Washington 99352, United States
[‡]Advanced Light Source, Lawrence Berkeley National Laboratory, Berkeley, California 94720, United States

**ABSTRACT:** Present and emerging biotechnological applications for iron (oxyhydr)oxide nanomaterials depend on their interaction with microorganisms, as do their toxicity, transport, and fate in biological and environmental systems. However, mass or electron transfer along key molecular pathways at microbe−nanomaterial interfaces is extremely difficult to quantify because of system complexity. Inspired by Fe(II)-oxidizing microbes widespread in nature, we isolate and characterize one such pathway by examining the oxidation of $Fe_{3-x}Ti_xO_4$ (magnetite-titanomagnetite) nanoparticles by the bacterial electron transfer enzyme MtoA, a decaheme *c*-type cytochrome. Oxidation by MtoA was studied as a function of the thermodynamic driving force for electron transfer by controlling the Ti(IV) doping content ($x$), which tunes the solid-state Fe(II)/Fe(III) ratio built into the nanoparticles. A higher Fe(II)/Fe(III) ratio appears to systematically increase the electron transfer kinetics to the cytochrome. In situ X-ray diffraction indicated that, during oxidation, the spinel ferrite lattice remains intact while structural Fe(II) is progressively depleted. Surface and atomic site specific Fe $L_{2,3}$-edge X-ray magnetic circular dichroism indicated that MtoA directly accesses magnetically ordered B-sublattice Fe(II) at the interface. This study provides the first quantitative insights into an isolated molecular pathway for biotransformation of iron (oxyhydr)oxide nanomaterials, and more generally, it also illustrates new techniques for probing these pathways in detail, featuring use of tailored nanoparticles, purified metalloenzyme, and synchrotron X-ray absorption spectroscopies.

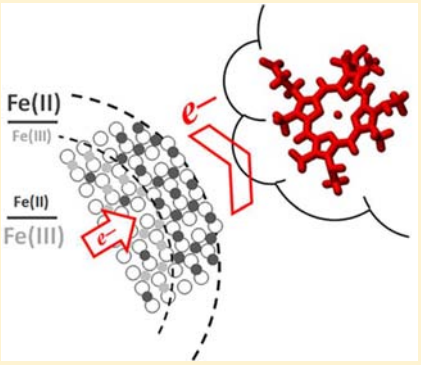


## INTRODUCTION

The toxicity, transport, and fate of redox-active nanomaterials in biological and environmental systems ultimately depend on their interaction with microorganisms.[1−4] Nanosized iron (oxyhydr)oxides are particularly important redox-active nanomaterials because of their many existing or promising roles in photoelectrochemical energy conversion,[5,6] medicine,[7,8] and nanobiotechnology[9,10] As just one recent example, the superparamagnetic properties of the nanoparticles under investigation in this study have been shown to improve particle quantification accuracy using magnetic resonance imaging (MRI) and magnetic particle detection (MPD) for in vivo studies on nanoparticle biokinetics and bioavailability.[11]

Because iron (oxyhydr)oxide nanoparticles are intrinsically abundant in the environment,[12,13] the study of their natural microbial synthesis and transformation pathways can be a foundation for new biological applications.[14] A major pathway involves linking cellular metabolism to the extracellular Fe(II)/Fe(III) redox couple, an energy acquisition strategy made possible by electron exchange across microbe−mineral interfaces. For example, at the near surface of the Earth, microbial oxidation of Fe(II) in aqueous or oxide form is pervasive. Fe(II) oxidation by neutrophilic iron-oxidizing bacteria (FeOB) can compete efficiently with abiotic oxidation, producing a variety of nanoparticulate Fe(III)-(oxyhydr)oxides. In turn, these Fe(III) products function as electron acceptors in deeper, anaerobic environments for dissimilatory Fe(III)-reducing bacteria (FeRB).[15−17] The characteristics, residence, and transformation of natural iron (oxyhydr)oxide nanomaterials are thus closely tied to these widespread classes of microorganisms.

Because the aqueous solubilities of Fe(II) and Fe(III) are very different at physiological pH, microorganisms have evolved complex biomolecular electron transfer machinery adapted to various iron forms. For instance, the Gram-negative bacterium *Sideroxydans lithotrophicus* ES-1 (ES-1) is a neutrophilic, lithotrophic FeOB originally isolated at the oxic−anoxic interface of Fe(II)-containing groundwater. ES-1 can respire on both aqueous and solid-phase forms of Fe(II) and is found closely associated with nanosized Fe(III)-(oxyhydr)oxide products.[18,19] The challenge for ES-1 and other FeOB is to oxidize Fe(II) without accumulating relatively insoluble Fe(III)-(oxyhydr)oxide nanoparticles inside the cell. Transmembrane electron transfer pathways that negate the need for Fe(II) uptake into the cell have been proposed. All involve heme-containing *c*-type cytochromes on the outer membrane to facilitate Fe(II) oxidation at the cell surface. To understand how ES-1 oxidizes Fe(II), the ES-1 genome was surveyed for candidate genes for extracellular Fe(II) oxidation. MtoA was

**Received:** February 11, 2013
**Published:** May 14, 2013

   dx.doi.org/10.1021/ja4015343 | *J. Am. Chem. Soc.* 2013, 135, 8896−8907

identified as a key decaheme *c*-type cytochrome that, together with MtoB and $CymA_{ES-1}$, form an assembly for electron transport from extracellular Fe(II) to the quinone pool in the bacterial inner membrane.[20,21] However, in whole cell form, oxidation of Fe(II) solid phases is extremely difficult to directly probe.[22] To date, no molecular-level information is available regarding the interaction between cytochrome and Fe(II)-containing phases.

Here, we aim for a fundamental advance by isolating this pathway, enabled by a well-defined nanoparticle system, purified cytochrome, and a novel set of tools, that provide molecular detail. We study the oxidation kinetics of spinel ferrite $Fe_{3-x}Ti_xO_4$ (magnetite-titanomagnetite) nanoparticles by MtoA in aqueous suspension. MtoA contains 10 heme cofactors; cyclic voltammetry in the pH range 7.1−9.2 indicated that the protein is redox active between ∼+100 and −400 mV (vs the standard hydrogen electrode (SHE)). MtoA has already been shown to oxidize aqueous Fe(II) complexes; the rate is sensitive to pH and the presence of Fe-complexing ligands.[21] Our $Fe_{3-x}Ti_xO_4$ nanoparticles, ∼100−120 Å in diameter, are synthesized with controlled Ti content ($x$) to tune the solid-state Fe(II)/Fe(III) redox potential across a desired range. Its natural preponderance and relevance aside,[23−27] biotechnological uses of magnetite ($x$ = 0) nanoparticles are vast,[14,28,29] and compositional tailoring ($x$ > 0) affords control of both the electronic and magnetic structure for new applications.[7,30] Replacement of Fe(III) by Ti(IV) in the lattice yields titanomagnetites, phase intermediates along the binary join between magnetite and ulvöspinel ($Fe_2TiO_4$). This substitution, occurring in the octahedral metal B sublattice, is accompanied by reduction of initially octahedral and then ultimately tetrahedral Fe(III) to Fe(II) for charge balance. Titanomagnetites thus have a "tunable" solid-state Fe(II)/Fe(III) ratio depending on selection of $x$. In analogy with the Nernstian half-cell potential, in which the free energy for an electron transfer reaction is related in part to the ratio of the activities of the reduced and oxidized species, that is, Fe(II) and Fe(III), respectively, this enables control of the thermodynamic reduction potential of the nanoparticles, allowing us to study its effect on the rate and extent of structural Fe(II) oxidation by MtoA.

Oxidation rates of $Fe_{3-x}Ti_xO_4$ nanoparticles ($x$ = 0, 0.15, and 0.38) by MtoA were measured under anaerobic conditions in real time using a stopped-flow system as a function of pH (7.3−9). Analogous batch reactions were conducted to provide sufficient reacted nanoparticle mass for detailed characterization. Nanoparticle suspensions before and after dilution and exposure to MtoA were measured in situ using micro-X-ray diffraction ($\mu$-XRD) to quantify changes in the Fe(II)/Fe(III) ratio within nanoparticle lattices. Changes in the Fe(II)/Fe(III) ratio and magnetic properties at the nanoparticle−cytochrome interface were characterized by synchrotron-based X-ray absorption (XA) and magnetic circular dichroism (XMCD) using the Fe $L_{2,3}$ absorption edge, in total electron yield mode for high surface-sensitivity. This study lays out first insights into heterogeneous biomolecular electron transfer and site-specific structural Fe(II) oxidation in nanosized Fe oxide nanoparticles by an important multiheme *c*-type cytochrome, with resolution down to a few angstroms at the interface.

## RESULTS AND DISCUSSION

**MtoA Adsorption.** Toward understanding the oxidation of $Fe_{3-x}Ti_xO_4$ nanoparticles by MtoA, we first needed to quantify amounts of MtoA that adsorb to the nanoparticles and any dependence of such on system variables. MtoA adsorption was studied in batch experiments in trisaminomethane (Tris) buffer solution at pH 7.3−9, by spectroscopically monitoring aqueous MtoA concentration changes. The absorption spectrum of oxidized MtoA exhibits a characteristic peak at 408 nm ($\alpha$ peak) with a shoulder at ∼352 nm and a weak absorption band at ∼530 nm. After complete reduction, the $\alpha$ peak shifts to 418 nm, and the shoulder peak shifts to 324 nm to form a distinct peak. In addition, two absorption peaks at 522 nm ($\beta$ peak) and 552 nm ($\gamma$ peak) appear.[21] These distinctive spectroscopic signatures allowed MtoA uptake onto the nanoparticles to be examined both with and without possible influence of the redox reaction. The percentages of the reduced MtoA remaining in solutions after sorption experiments are shown in Figure 1. The

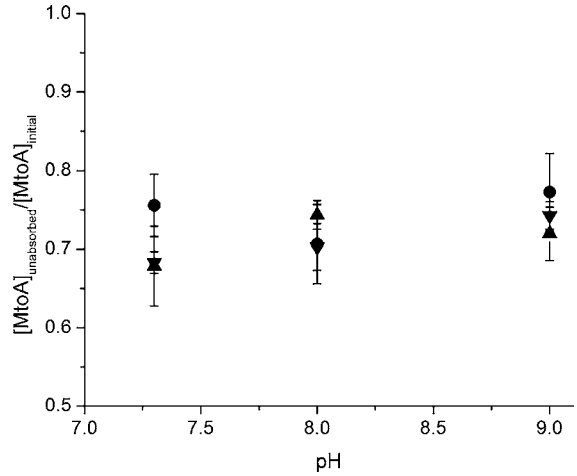


**Figure 1.** Ratios of concentration of reduced MtoA remaining in solution to initial MtoA concentration (∼0.8 $\mu$M) after adsorption onto $Fe_{3-x}Ti_xO_4$ nanoparticles containing 108 ± 4 $\mu$M Fe(II) equivalents in Tris buffer solution at pH 7.3−9 (●, $x$ = 0; ▲, $x$ = 0.15; ▼, $x$ = 0.38). Error bars represent one standard deviation from three replicate experiments.

results were calculated from the absorbance at both 552 and 418 nm to confirm that no peak shifts related to the reduction occurred and that the decrease in absorbance was solely a result of MtoA adsorption. The percentage of adsorbed MtoA was similar within error (23−32%) for all measurements regardless of Fe(II)/Fe(III) ratios ($x$) in the nanoparticles or pH value (Figure 1). Previous studies revealed that protein adsorption on nanoparticles is mainly affected by size, shape, composition, crystallinity, surface area, and surface properties of nanoparticles.[31] Transmission electron microscopy (TEM) and Brunauer−Emmett−Teller (BET) analysis showed that the $Fe_{3-x}Ti_xO_4$ nanoparticles with different $x$ values have no significant difference in size, shape, surface roughness, and specific surface area,[32] consistent with no observed effect on MtoA adsorptivity. The selected range of pH values in the experimental solutions is above the point of zero charge (PZC) for all the nanoparticles used in this study ($pH_{PZC}$ ∼ 6−7).[32] Consequently, the influence of pH on protein sorption, either through changes in surface charge or aggregation extent of the nanoparticles, is expected to be insignificant. Thus, in our studies of $Fe_{3-x}Ti_xO_4$ nanoparticle oxidation by MtoA, the amount adsorbed can be assumed constant, independent of system variables and reaction extent.


dx.doi.org/10.1021/ja4015343 | J. Am. Chem. Soc. 2013, 135, 8896−8907

**Nanoparticle Release of Fe(II)(aq).** It was also important to understand the extent to which pH changes can alter the nanoparticles through acidic dissolution, a process that oxidizes the particles by releasing Fe(II) into solution, according to the following:

$$Fe^{3+}Fe^{3+}Fe^{2+}O_4^{2-} + 2H^+ \rightarrow \frac{3}{4}Fe^{3+}Fe^{3+}_{5/3}\square_{1/3}O_4^{2-} + H_2O + Fe^{2+} \quad (1)$$

The symbol □ represents cationic vacancies that accumulate in the structure due to diffusive migration of iron cations out of the octahedral sublattice concurrent with oxidation at a rate of one vacancy created per three electrons removed from the solid. Studies of Fe(II)(aq) release provided a means to estimate the extent of preoxidation of the nanoparticles as a result of dissolution prior to the addition of MtoA and to estimate aqueous Fe(II) concentrations competing with structural Fe(II) in the nanoparticles during the nanoparticle oxidation by MtoA. Fe(II)(aq) release from the nanoparticles was quantified by diluting a concentrated stock suspension of the nanoparticles at pH ∼ 8.5, in which less than 1 μmol of aqueous Fe(II) was released per gram of nanoparticles in suspension[32] to produce buffered solutions with different pH values. The equilibrated concentrations of aqueous Fe(II) released from the $Fe_{3-x}Ti_xO_4$ nanoparticles at pH 7.3−9 are shown in Figure 2. As anticipated from eq 1, the extent of

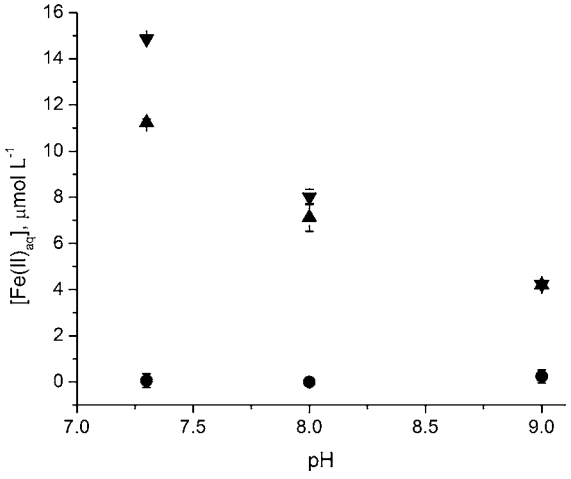


**Figure 2.** Concentration of Fe(II) released from $Fe_{3-x}Ti_xO_4$ nanoparticles as a function of pH values (●, $x$ = 0; ▲, $x$ = 0.15; ▼, $x$ = 0.38). Error bars represent one standard deviation from three replicate experiments.

Fe(II) release expectedly decreases with increasing pH. Fe(II) release was also strongly dependent on $x$; negligible amounts of Fe(II) were released from 0.025 g/L of $Fe_3O_4$ nanoparticles ($x$ = 0), under all pH conditions, and increasing amounts of Fe(II) were released with increasing $x$ in suspensions with the same nanoparticle density. The same trend was previously observed in the dissolution of $Fe_{3-x}Ti_xO_4$ nanoparticles ($x$ = 0−0.67) at pH 8.[32] Thus, although multiple pH values were used in the experiments with MtoA, because both the total Fe(II) and the associated aqueous Fe(II) concentrations were independently known, ranging from below the detection limit to on the order of available MtoA heme groups, competing effects of homogeneous versus heterogeneous electron transfer to MtoA could be measured.

It is furthermore noteworthy that this equilibration process between the Fe(II) content in the nanoparticles and that partitioned into solution is also accompanied by a heterogeneous redistribution of Fe(II) within the nanoparticles themselves. During release, dilution in an oxidative[33] or acidic[34,35] solution also appears to enhance the B-site Fe(II)/Fe(III) ratio near the surface relative to the interior. This preferential redistribution occurs nominally at a rate of one Fe removed (one vacancy inserted) for every three electrons mobilized to the interface, persisting through acidic dissolution up to stoichiometric phase stability limits for a given value of $x$.[32]

**Effect of pH on Nanoparticle Oxidation by MtoA.** We studied the rate and extent of nanoparticle oxidation by MtoA as a function of $x$ and pH, using a stopped-flow reactor with less than 1 ms deadtime and absorbance data recorded at 50 ms time intervals. For comparison, using the same method, MtoA oxidation kinetics of aqueous Fe(II) ($FeCl_2$) in the absence of nanoparticles was also performed. To facilitate the comparison, the total Fe(II) concentration used in all experiments was selected to be approximately equal (108 ± 4 μM), such that the initial concentration of Fe(II) in each of the $Fe_{3-x}Ti_xO_4$ nanoparticle experiments was the same, as was the initial concentration of $FeCl_2$ in the experiments without nanoparticles. The reaction kinetics were studied by monitoring the change in absorbance for MtoA at 552 nm. The concentration of oxidized MtoA calculated from the measured absorbance at 552 nm as a function of time is shown in Figure 3. Control experiments were performed by mixing oxidized MtoA and buffer solution, without a reductant, at the desired pH. No obvious change in absorption spectra was observed in all control experiments. This indicated that MtoA was not denatured or otherwise deactivated under the experimental conditions within the measured time course.

The results show that pH is a key master variable in this system. More MtoA was reduced, hence more Fe(II) oxidized, at the higher pH value, in reactions with solely aqueous Fe(II) and those containing nanoparticles (Figure 3). The redox potential and adsorptivity of MtoA to our nanoparticles is already known to be independent of pH over the measured range.[21] Consequently, the pH effect must be related to the iron chemistry, despite necessary differences between the homogeneous versus heterogeneous cases. In the homogeneous reaction, higher reactivity at higher pH can be attributed to differences in aqueous Fe(II) speciation, namely, to a higher expected initial concentration of the more reactive species $Fe(OH)^+$ in solution. The percentage of $Fe(OH)^+$ in 108 μM $FeCl_2$ solution (with 150 mM NaCl) increases from ∼0.3% at pH 7.3 to ∼12% at pH 9; the same percentages as for the 18 μM $FeCl_2$ solution used in previous work on the homogeneous Fe(II)−MtoA system.[21] It is well recognized that $Fe(OH)^+$ is a stronger reductant (lower reduction potential) than aqueous $Fe^{2+}$.[36,37] Furthermore, upon initial Fe(II)(aq) oxidation, Fe(III) solid-phase product is expectedly present, although here found to be below the detection limit in all cases (∼0.004 mM[38]), that nonetheless provides a reactive surface with which to heterogeneously catalyze further Fe(II)(aq) oxidation by MtoA. Fe(II) sorbed to Fe(III) (oxyhydr)oxides has been shown to be a more strongly reducing form of Fe(II).[39,40]

For the case when nanoparticles are present, various pH effects on the solid-phase Fe(II) are also at play. For example, in the reaction between MtoA and pure magnetite nanoparticles ($x$ = 0), aqueous Fe(II) is expected to be below the

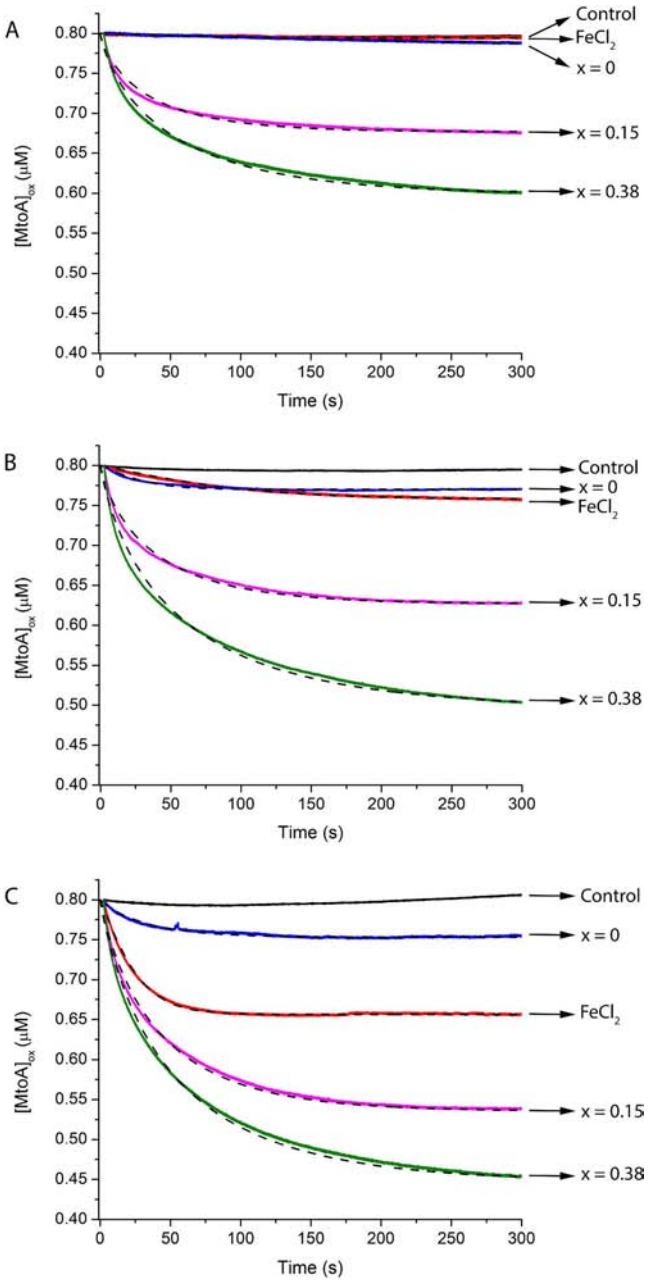


**Figure 3.** Variation of the concentration of purified MtoA as a function of time during the control experiments (black) and during the oxidation of $FeCl_2$ (red), $Fe_3O_4$ nanoparticles (blue), $Fe_{2.85}Ti_{0.15}O_4$ nanoparticles (purple), and $Fe_{2.62}Ti_{0.38}O_4$ (green) at pHs 7.3 (A), 8 (B), and 9 (C). The fitting curves are shown as black dashed lines.

detection limits over the measured pH range (less than ~0.004 mM); thus, only structural Fe(II) in the nanoparticles was available for reaction. The rate and extent of MtoA reduction by these nanoparticles increased slightly with increasing pH (Figure 3). A similar trend was observed with the $x > 0$ $Fe_{3-x}Ti_xO_4$ nanoparticles, but in these cases, an attendant Fe(II)(aq) fraction with independent pH effects as above are also relevant.

The pH effect on structural Fe(II) may be conceptually understood as underlain by several processes. First is the formation of surface complexes between nanoparticle Fe sites and $OH^-$. At pH 7.3, the nanoparticles are close to the PZC, whereas at pH 8 and 9, they develop a stronger net negative charge[41,42] because the elevated pH increases the $OH^-$ activity at the surface. Similar to what is expected for $Fe(OH)^+$, the accumulation of strong nucleophile $OH^-$ ligands at Fe sites, forming >Fe−$OH^-$ groups, shifts electron density into Fe and increases the reducing power of Fe(II) at the surface. The redox potential of magnetite suspensions has been shown to decline linearly with increasing pH,[42−45] increasing the exergonicity of the electron transfer reaction. Consistent with this picture, it is known that increasing pH enhances the thermodynamic stability of Fe(III) products relative to Fe(II) forms.[46] Lastly, while not affecting the adsorbed density of MtoA, these negatively charged surface complexes may also provide sites capable of facilitating closer electronic interaction of MtoA with surface Fe(II) through bridging $OH^-$ ligands.[40] Collectively, these effects enhance heterogeneous electron transfer efficiency from structural Fe(II) to MtoA with increasing pH and in vivo would consequently also promote microbial oxidation of these nanoparticles.

**Effect of Fe(II)/Fe(III) Ratio in Nanoparticle Oxidation by MtoA.** In the case of nanoparticles with $x > 0$, both solid-phase and aqueous Fe(II) were present, in known relative concentrations. The oxidation rates and extent of oxidation of these nanoparticles were much higher than those of the $FeCl_2$ solutions and of the $x = 0$ nanoparticle suspensions, all with the same initial total Fe(II) concentration under the same experimental conditions (Figure 3). Although, at pH 7.3 for all nonzero values of $x$, the concentration of Fe(II) released into solution was sufficient in principle to reduce the majority of the MtoA, the faster rates compared with those for $FeCl_2$ imply that structural Fe(II) oxidation by MtoA was more important and efficient than oxidation of associated Fe(II)(aq). It is furthermore evident that the redox reactivity of the nanoparticles appears more strongly and systematically dependent on the proportion of Fe(II) relative to Fe(III) in the solid, rather than on the absolute Fe(II) concentration within. By design, initial nanoparticle amounts were mass adjusted such that the total Fe(II) concentration provided to the system to react with MtoA was the same in each experiment. With increasing $x$ from $x = 0$ up to $x = 0.38$, although Ti(IV) substitution rapidly increases the molar ratio of Fe(II) to Fe(III) per formula unit (50% increase), the lattice Fe(II)

**Table 1. Summary of Characteristics of $Fe_{3-x}Ti_xO_4$ Nanoparticles before and after Reactions**

| | | | | XRD Fe(II)/Fe(III) | | | | | | XMCD Fe(II) /Fe(III) | | | | | |
|---|---|---|---|---|---|---|---|---|---|---|---|---|---|---|---|
| | | | | before MtoA | | | after MtoA | | | before MtoA | | | after MtoA | | |
| $x$ | size (Å) | SSA ($m^2/g$) | initial [Fe(II)] (mmol/g) | pH 7.3 | pH 8 | pH 9 | pH 7.3 | pH 8 | pH 9 | pH 7.3 | pH 8 | pH 9 | pH 7.3 | pH 8 | pH 9 |
| 0.00 | 118 | 98.2 | 4.42 | 0.46 | 0.46 | 0.46 | 0.45 | 0.45 | 0.45 | 0.64 | 0.69 | 0.67 | 0.62 | 0.27 | 0.20 |
| 0.15 | 94 | 121.3 | 4.44 | 0.56 | 0.57 | 0.57 | 0.55 | 0.57 | 0.56 | 0.59 | 0.61 | 0.70 | 0.48 | 0.24 | 0.23 |
| 0.38 | 106 | 117.3 | 4.76 | 0.66 | 0.70 | 0.69 | 0.64 | 0.65 | 0.66 | 0.72 | 0.89 | 0.90 | 0.61 | 0.34 | 0.32 |


dx.doi.org/10.1021/ja4015343 | J. Am. Chem. Soc. 2013, 135, 8896−8907

concentration increases only slightly, on both a density basis (6% increase in moles of Fe(II) per unit volume) and a mass basis (8% increase in moles of Fe(II) per unit mass; Table 1).[32] The relatively low sensitivity of the former to Ti content arises in part because of a cancellation effect from the concomitant increase in the unit cell volume with increasing $x$ and the latter because of the similar atomic masses of Ti and Fe. Furthermore, because the Ti-bearing nanoparticles have a smaller mean diameter than the $x = 0$ nanoparticles (Table 1), the mass adjustment for constant total Fe(II) concentration (for higher $x$, fewer nanoparticles but of intrinsically higher surface area) also yields statistically insignificant solid surface area differences between each experiment (2.4, 3.0, and 2.7 $m^2$/L for $x = 0$, 0.15, and 0.38, respectively). Therefore, the systematically increased MtoA reduction rate observed for $x > 0$ nanoparticles begins to suggest that it is the increase in the Fe(II)/Fe(III) ratio in the solid phase that results in a faster electron transfer reaction to MtoA, similar to previous observations of faster Tc(VII) reduction with increasing $x$ in these same materials.[38] An increase in this ratio yields a systematically lower reduction potential built into the solid, as was previously established for the magnetite-maghemite ($Fe^{8}_{3}O_4$) solid solution series by, for example, comparing open circuit potentials to Fe(II)/Fe(III) stoichiometry.[43−45,47,48]

To examine these relationships further, the data in Figure 3 were fit using an equilibrium-constrained, second-order kinetic model that describes the reaction rate as proportional to the concentration of Fe(II), supplied either as $FeCl_2$ solution or as $Fe_{3-x}Ti_xO_4$ nanoparticles, and MtoA (see the Experimental Methods section). Least-squares fits to the data yielded second-order rate constants ($k$), conditional equilibrium constants ($K_{eq}$), and the reaction nonlinearity order ($n$). The nonlinearity order for the reactions in homogeneous solution with $FeCl_2$ is 1, but it is 0.12−0.25 for the reactions with nanoparticles, suggesting a more complex reaction pathway than the second-order redox interaction in the heterogeneous case. Although at the reaction onset the concentration of Fe(II) in the nanoparticles and $FeCl_2$ was more than 10 times the oxidized heme concentration provided by the MtoA, the extent of MtoA reduction was incomplete in all experiments. Similar incomplete MtoA reduction was observed in reactions with aqueous Fe(II) complexes in homogeneous solution.[21] The most likely reason is that the redox potential difference between the nanoparticles and MtoA decreases to zero, that is, equilibrium is reached, before all the MtoA reacts, as the concentration of Fe(II) in the nanoparticles decreases and the concentration of reduced MtoA increases over the course of the reaction. In Figure 4, fitted rate and equilibrium constants for reactions between MtoA and the $Fe_{3-x}Ti_xO_4$ nanoparticles are plotted against the structural Fe(II)/Fe(III) ratio in the nanoparticles before reaction, as determined by $\mu$-XRD and the known systematic correlation between the unit cell constant and the Fe(II)/Fe(III) ratio.[32] There is a general trend of increasing rate (Figure 4A) and conditional equilibrium constant (Figure 4B) with both increasing pH and Fe(II)/Fe(III) ratio. While the rates show a nonlinear dependence, the conditional equilibrium constants are nearly linearly correlated to the initial Fe(II)/Fe(III) ratio across our experimental conditions. The latter trend is expected if the Fe(II)/Fe(III) ratio is indeed the quantity controlling the extent of the reaction, by setting the thermodynamic driving force for electron transfer from the

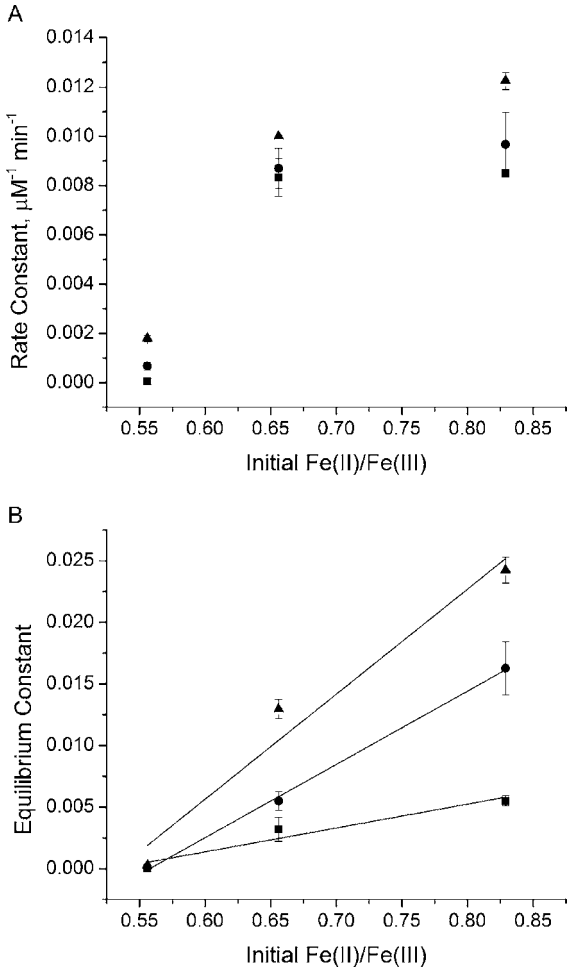


**Figure 4.** Rate constants (A) and equilibrium constants (B) of the reaction between MtoA and $Fe_{3-x}Ti_xO_4$ nanoparticles as a function of the initial Fe(II)/Fe(III) ratio in the solid derived from stopped-flow data shown in Figure 3 (■, pH 7.3; ●, pH 8; ▲, pH 9). Error bars represent one standard deviation from three replicate experiments.

nanoparticles to MtoA. Although this analysis does not enable a standard reduction potential to be determined for the nanoparticles, the range of reduction potentials as a function of $x$ and pH can be assessed through the relationship between reaction free energy ($\Delta G_r'$) and the cell potential ($\Delta E_r'$):

$$\Delta G_r' = -RT\ln K_{eq} = -mF\Delta E_r' \quad (2)$$

in which $R$ is the gas constant, $T$ is the temperature, $m$ is the number of electrons transferred, and $F$ is the Faraday constant. The redox potential of MtoA was approximately the same in all the reactions for our conditions, ranging from ∼+100 to −400 mV but with an average midpoint potential of approximately −130 mV versus SHE.[21] The difference in $\Delta E_r'$ is thus due to the different redox potentials of the nanoparticles, which by deduction from eq 2 spanned 240 mV between $x = 0$ and $x = 0.38$, with $x = 0.38$ nanoparticles at the lowest relative redox potential in the series. The slight nonlinearity of the conditional equilibrium constants with respect to the Fe(II)/Fe(III) ratio (Figure 4B) can be explained by the nonlinear $x$ dependence of the free energy of mixing in the $Fe_3O_4$−$Fe_2TiO_4$ solid solution, as described by Lilova et al.[49] The free energy of mixing is a small positive quantity that is parabolic (symmetric) with respect to $x$; thus, the relative thermodynamic stability of


dx.doi.org/10.1021/ja4015343 | J. Am. Chem. Soc. 2013, 135, 8896−8907

intermediate compositions in the series approaches a minimum nonlinearly between $0 \leq x \leq 0.5$. The subtle deviation from linearity for the conditional equilibrium constants is in the correct direction given the curvature of the mixing free energy nonlinearity. There thus appears to be a direct correlation between reaction driving force and the Fe(II)/Fe(III) ratio in the nanoparticles. In this regard, although a non-negligible fraction of MtoA is reduced in the $FeCl_2$ control experiments at higher pH values (Figure 3B,C), aqueous Fe(II) appears not to play a determining role in our system overall, for several reasons. First, as described, the MtoA reduction extent is systematically correlated with $x$. Second, for $x > 0$ nanoparticles, the MtoA reduction extent is always much greater than that in the homogeneous $FeCl_2$ control despite the fact that the attendant Fe(II)(aq) concentrations with these nanoparticles are more than seven times less than in the control (Figure 2). Third, there is a systematic reduction rate and extent differentiation between $x = 0.15$ and 0.38 samples at higher pH values even though their associated Fe(II)(aq) concentrations are identical. The heterogeneous electron transfer pathway thus seems to be the more important control in MtoA reduction.

Now with respect to the rate constant dependence on the Fe(II)/Fe(III) ratio, a systematic trend is also apparent (Figure 4A). The second-order rate constant increases with an exponentially decaying dependence on an increasing Fe(II)/Fe(III) ratio. Although no relationship between thermodynamic driving force and reaction kinetics can be intrinsically presumed, there are cases where the interdependence is defined and it is qualitatively applicable to the present system. One such case is Marcus' theory of electron transfer, in which the free energy of activation for electron transfer has a quadratic dependence on the reaction free energy.[50] At any given pH, in the electron transfer reaction from nanoparticles to MtoA during residence in the adsorbed state, the so-called encounter complex, if we assume a constant reorganization energy and electronic coupling matrix element (in the weak-coupling limit), the observed trend between rate constant and Fe(II)/Fe(III) ratio is consistent with a Marcus description. The rate increases with increasing exergonicity (i.e., increasing Fe(II)/Fe(III) ratio) and exponentially approaches a maximum rate as the magnitude of the reaction free energy nears the value of the reorganization energy, as expected from the normal region behavior of Marcus theory. Though just one framework with which to understand the observed trend, and further research is needed, the conceptual agreement is consistent with the Fe(II)/Fe(III) ratio in the nanoparticles as the rate-controlling quantity in our system.

**Nanoparticle–MtoA Electron Transfer.** To gain mechanistic insight into how MtoA accesses Fe(II) in the nanoparticles, batch experiments were performed under conditions identical to those used in the stopped-flow method, which allowed us to obtain sufficient product material for characterization by $\mu$-XRD and XMCD. To assess correspondence between the batch and stopped-flow experiments, the change in Fe(II) concentration in the nanoparticle suspensions at the end of the reaction was calculated from the concentration of MtoA that was reduced and was plotted as a function of the initial Fe(II)/Fe(III) ratio in the nanoparticles at the different pH values (Figure 5). The observed trend is in agreement with that for the conditional equilibrium constants in Figure 4, indicating good correspondence between the two experimental approaches. Samples of $x = 0$ nanoparticles analyzed by $\mu$-XRD

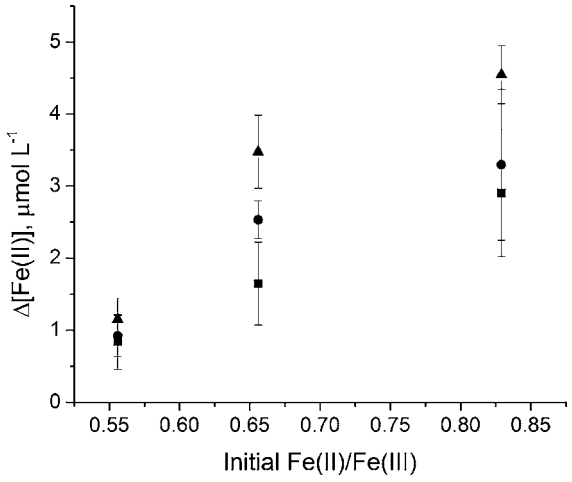


**Figure 5.** Change of [Fe(II)] in $Fe_{3-x}Ti_xO_4$ nanoparticles during oxidation by MtoA as a function of the initial Fe(II)/Fe(III) ratio in the solid (■, pH 7.3; ●, pH 8; ▲, pH 9). Error bars represent one standard deviation from three replicate experiments.

under anoxic conditions in aqueous suspension before and after reaction with MtoA at pH 9 show that no new phases were produced; the only peaks present corresponded to magnetite (Figure 6). A shift of peak positions toward higher 2Θ values

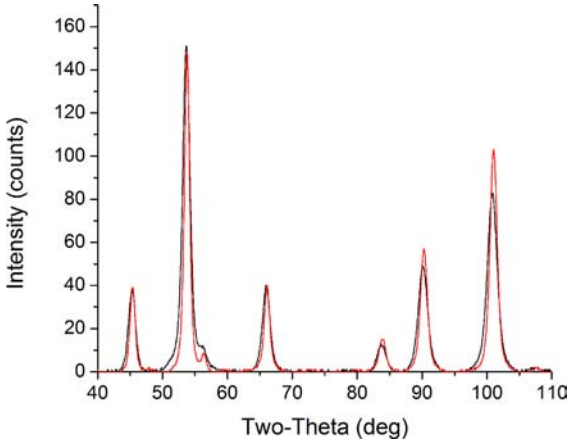


**Figure 6.** $\mu$-XRD of $Fe_3O_4$ nanoparticles before (black) and after (red) reaction with 0.8 $\mu$M MtoA.

was observed in all nanoparticles after the reaction, and using the systematic relationship between the unit cell constant and the Fe(II)/Fe(III) ratio mentioned above,[32] the change in the Fe(II)/Fe(III) ratio in the reacted nanoparticles was calculated (Table 1). In all experiments, the structural Fe(II)/Fe(III) ratio decreased after reaction, indicating that structural Fe(II) was directly accessed and oxidized by MtoA. The decrease in the $\mu$-XRD detectable Fe(II)/Fe(III) ratio was larger for $x > 0$ samples, in agreement with the greater observed extent of reduction of MtoA with these nanoparticles.

The nanoparticles before and after reaction with MtoA were also analyzed using XA and XMCD at the Fe $L_{2,3}$ edge and the Ti $L_{2,3}$ edge. XA provides a measure of total Fe, and XMCD is a function of the magnetic Fe component of the sample, sensitive with A- and B-site specificity to structural Fe(II) and Fe(III). Because the signal was collected in total electron yield mode, both techniques emphasize information from the topmost several angstroms of the nanoparticle surfaces (more detail is


dx.doi.org/10.1021/ja4015343 | J. Am. Chem. Soc. 2013, 135, 8896–8907

provided in the Experimental Methods section).[51] The XMCD spectra for nanoparticles before and after reaction with MtoA at pHs 7.3, 8, and 9 are shown in Figure 7A ($x$ = 0), B ($x$ = 0.15), and C ($x$ = 0.38). Measured XMCD spectra for the nanoparticles have three main features: B-site Fe(II) (negative peak at ∼708 eV), A-site Fe(III) (positive peak at ∼709.5 eV), and B-site Fe(III) (negative peak at ∼710.5 eV). According to calculated spectra for these three main components in magnetite,[52,53] the experimental XMCD spectrum was fit to produce occupancy ratios for the proportions of Fe(II) and Fe(III) in the B site and Fe(III) in the A site. Fe(II)/Fe(III) ratios for titanomagnetite nanoparticles before and after reaction, calculated from the XMCD spectra, are shown in Table 1. The Fe(II)/Fe(III) ratio at the surface decreased after reaction for all values of $x$ and at each pH, indicating that magnetically ordered surface Fe(II) was accessed and oxidized by MtoA. This can be seen in Figure 7A–C by a decrease in the peak corresponding to B-site Fe(II).

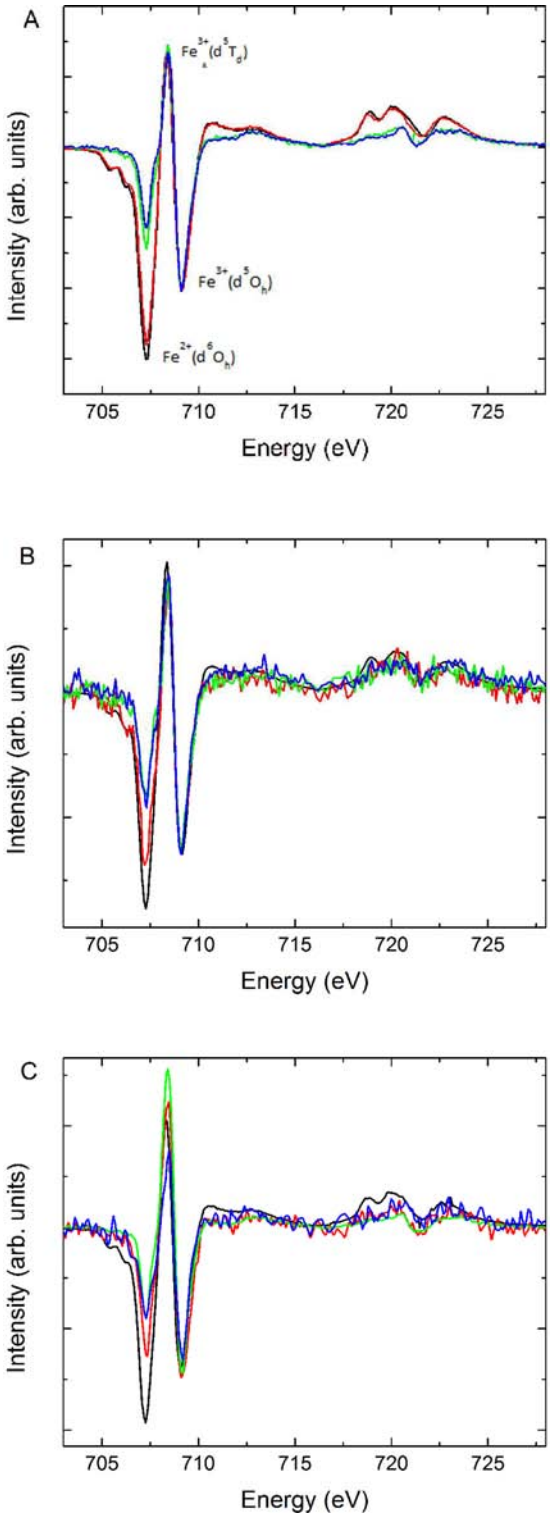


**Figure 7.** XMCD spectra of $Fe_{3-x}Ti_xO_4$ nanoparticles (A, $x$ = 0; B, $x$ = 0.15; C, $x$ = 0.38) before (black line) and after reaction with 0.8 $\mu$M MtoA at pH 7.3 (red line), pH 8 (green line), and pH 9 (blue line).

The $\mu$-XRD/XMCD data also show that nanoparticle oxidation by MtoA is mechanistically distinct from oxidation by acidic dissolution (eq 1). Figure 8 shows the effect of pH-dependent Fe(II)(aq) release upon dilution from the concentrated stock suspension on the Fe(II)/Fe(III) ratio in the nanoparticles both in the bulk and at the surface, as measured by $\mu$-XRD and XMCD, respectively. Dissolution has the most significant effect on the Fe(II) in the interior of the nanoparticles with a significant decrease in the $\mu$-XRD Fe(II)/Fe(III) ratio occurring as a result. After oxidation with MtoA, only a subtle further decrease in the $\mu$-XRD Fe(II)/Fe(III) ratio is observed. The changes in $\mu$-XRD Fe(II)/Fe(III) ratio in both cases are also shown to be insensitive to pH. In contrast, as indicated by XMCD, at the surface while dissolution tends to only slightly adjust the Fe(II)/Fe(III) ratio, subsequent oxidation by MtoA yields a substantial decrease in the surface Fe(II)/Fe(III) ratio in all cases except for $x$ = 0 nanoparticles, particularly at the higher pH values (Figure 8). This distinction can be explained by the fact that, while oxidation by dissolution produces an oxidized interior and a surface region enriched in Fe(II) relative to Fe(III), this redistribution is coupled only to loss of extractable Fe(II) to solution and does not simultaneously accumulate an Fe(III) product at the surface. In contrast, oxidation by MtoA directly accesses and converts surface-enriched Fe(II) to Fe(III), and this simultaneous accumulation of an Fe(III) product at the surface results in a larger net decrease in the surface Fe(II)/Fe(III) ratio.

The XMCD data allow us to further elaborate on the apparent pH dependence of nanoparticle oxidation by MtoA, with respect to the Fe(II)/Fe(III) ratio at the surface and the thermodynamic driving force for electron transfer. The dissolution step causes partial oxidation of the nanoparticles with enrichment of Fe(II) to the surface. As the results in Figure 2 show, while dissolution releases Fe(II) into solution, lower quantities are released as the pH increases. However, the $\mu$-XRD results showed that similar amounts of Fe(II) were lost from the structure over the experimental pH range. Thus, more Fe(II) enrichment was present at the surface of the nanoparticles at higher pH, as shown by the increase in the XMCD Fe(II)/Fe(III) ratio with increasing pH after dissolution (Figure 8). Along with expected pH effects on the nanoparticle surface chemistry discussed above, the increase in the concentration of this magnetically ordered structural Fe(II) at the nanoparticle surface relative to Fe(III) correlates with the increased reactivity with MtoA at higher pH. The greatest change in the nanoparticles for all values of $x$ occurred between pHs 7.3 and 8, with the XMCD spectra for the samples measured at pHs 8 and 9 remaining quite similar. At pH 7.3, the nanoparticles are close to their PZC, but at pHs 8 and 9, as discussed above, the nanoparticles develop a net negatively charged surface through adsorption of $OH^-$ ions. The XRD


dx.doi.org/10.1021/ja4015343 | J. Am. Chem. Soc. 2013, 135, 8896–8907

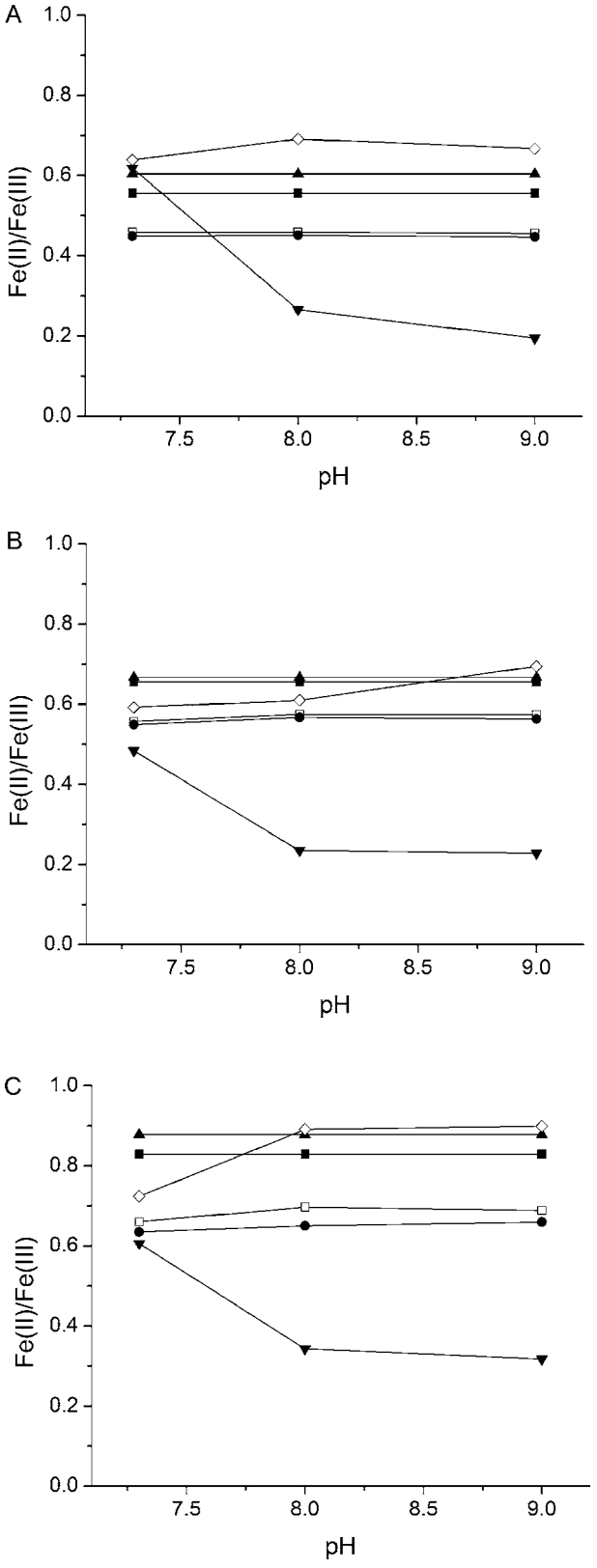


**Figure 8.** Fe(II)/Fe(III) ratio for $Fe_{3-x}Ti_xO_4$ nanoparticles (A, $x$ = 0; B, $x$ = 0.15; C, $x$ = 0.38), as a function of pH, as measured by $\mu$-XRD before dissolution (■), after dissolution (□), and after oxidation with MtoA (●) and as measured by XMCD before dissolution (▲), after dissolution (◊), and after oxidation with MtoA (▼).

Fe(II)/Fe(III) ratio was not significantly affected by the presence of MtoA as the concentration of MtoA was not sufficient to oxidize all of the Fe(II) that had been enriched to the surface as a result of dissolution; therefore, the driving force for further spontaneous solid-state migration of Fe(II) from the interior to the interface was insignificant.

Considering that the ratio of MtoA to nanoparticles was small (0.8 $\mu$M of MtoA, with the capacity to oxidize 8 $\mu$M Fe(II) to 108 $\mu$M total Fe(II) in the nanoparticles) and based on the large change in the XMCD Fe(II)/Fe(III) ratio, it is clear that MtoA contact with the nanoparticles has a substantial effect. Figure 1 shows that ∼30% of the available MtoA was sorbed onto the nanoparticles; this sorbed fraction had a significant impact on the intensity of the XA spectra, evident at both the Fe and the Ti L edges. For example, the Fe XA spectra decreased in intensity on average by an order of magnitude after exposure to MtoA. The reduction in intensity of the XA is consistent with signal attenuation due to protein covering the nanoparticle surfaces, which in turn further enhances the surface sensitivity of the L-edge information coming from the nanoparticles, and the spectra in Figure 7 are thus representative of only the top few, highly oxidized surface layers. The Ti L-edge signal disappeared entirely after exposure to MtoA. The more complete attenuation of the Ti signal is unlikely dependent on an Fe signal contribution from heme Fe in MtoA because of its low sorbed density, which further supports the interpretation that the oxidative process involves B-sublattice diffusion of Fe(II) to the surface and oxidation in-site by MtoA, leaving an Fe(III)-rich surface phase that is relatively deficient in Ti.

Because the ratio of MtoA to $Fe_{3-x}Ti_xO_4$ nanoparticles was small, investigation of the electron balance was not practical. To overcome this problem, an experiment was carried out with $x$ = 0.38 nanoparticles at pH 7.6, using a 10× higher concentration of MtoA at ∼8 $\mu$M, giving an oxidation capacity of 80 $\mu$M Fe(II) to 108 $\mu$M Fe(II) in the nanoparticles. Calculation of the amount of Fe(II) lost from the nanoparticle structure from the change in the Fe(II)/Fe(III) ratio as measured by $\mu$-XRD gave a concentration of 29.0 $\mu$M. According to spectroscopic results, in this experiment, 5.6% of the MtoA was absorbed on nanoparticles, which when normalized for the 10× higher MtoA concentration, yields amounts adsorbed comparable to the main experiments described above, and 10.0% of the MtoA left in solution was reduced. If it is assumed that all of the absorbed MtoA was reduced, this gives a total oxidized Fe(II) concentration of 12.5 $\mu$M from the nanoparticles in this experiment, which scales well compared to 2.4 $\mu$M deduced similarly for the analogous experiment described above at 10× lower MtoA concentration (pH = 7.3; $x$ = 0.38). The 12.5 $\mu$M estimate for consumed nanoparticle Fe(II) based on MtoA UV−visible (UV−vis) spectroscopy compares well in order of magnitude with the 29 $\mu$M $\mu$-XRD-based estimate. The difference is also of the correct sign, because it is probable that a fraction of Fe(II) lost from the structure could be present at the surface in a disordered state that is not measurable by $\mu$-XRD, and where it would potentially be sterically inaccessible to the remaining oxidized MtoA in solution due to the presence of a protective layer of reduced MtoA that covered nanoparticle surfaces.

## ■ CONCLUSIONS

This study provides new and direct molecular-level information on electron transfer across an iron (oxyhydr)oxide nanoma-


dx.doi.org/10.1021/ja4015343 | J. Am. Chem. Soc. 2013, 135, 8896−8907

terial−cytochrome interface, inspired by a natural FeOB microbial system but with implications and relevance ranging from environmental toxicity to biotechnological applications. By use of well-defined compositionally tuned spinel ferrite nanoparticles, we were able to obtain fundamental insight into the roles of solid-state redox potential, solid-state Fe atom and electron redistribution, site selectivity, and pH in the oxidation of $Fe_{3-x}Ti_xO_4$ nanoparticles by an important metalloenzyme. With respect to respiration pathways of FeOB, this study helps validate the hypothesis that extracellular Fe(II) can be accessed directly by organisms such as ES-1 via transmembrane heme-containing electron transfer proteins interacting with nanosized (oxyhydr)oxides. These proteins appear capable of extracting the reactive Fe(II) fraction from within the solid, in this case from ferrite spinel nanoparticles, by coupled electron and cation diffusion through the solid to the interface with MtoA, resulting in a topotactic transformation of these materials to a more oxidized but structurally similar form. The extent of electron bioavailability is controlled by the solid-state redox potential, defined by the Fe(II)/Fe(III) ratio in the structure. We also show that, in complex systems such as these that involve quantification of large changes in small concentrations of biological reactant, as well as quantification of the relatively small changes in the Fe(II)/Fe(III) content in the nanomaterials, an integrated multimethod approach is required. The use of the compositionally controlled nanoparticles, in combination with in situ $\mu$-XRD and surface-sensitive XA/XMCD was pivotal to elucidate details of the electron transfer reaction.

## EXPERIMENTAL METHODS

**$Fe_{3-x}Ti_xO_4$ Nanoparticle Synthesis.** Nanoparticles were prepared under ambient conditions in aqueous suspension by coprecipitating a stoichiometric mixture of $FeCl_2$, $FeCl_3$, and $TiCl_4$ in 0.3 M HCl (pH < 1) with ammonium ($NH_4OH$) solution in an anoxic glovebox ($N_2$ atmosphere from $LN_2$ boil-off; lower than 1 ppm residual $O_2$; hereafter referred to as the glovebox) such that

$$(1 + x)Fe^{2+} + (2 - 2x)Fe^{3+} + xTi^{4+} + 8OH^- \rightarrow Fe_{3-x}Ti_xO_4 + 4H_2O \quad (3)$$

The nanoparticles were magnetically separated from the aqueous phase and washed twice with degassed and deionized milli-Q (>18 MΩ cm resistivity) water (DDW) to remove possible impurities such as residual metal chlorides. After washing, the nanoparticles were resuspended in water prepared equivalently and stored inside the glovebox.

Synthesis and characterization of $Fe_{3-x}Ti_xO_4$ nanoparticles in the range $0 \leq x \leq 0.6$ were reported in detail in Pearce et al.[32] In the present study, nanoparticles with $x = 0$, 0.15, and 0.38 were used. The suspension density was determined, and the chemical composition of the nanoparticles, in terms of Fe(II) and total Fe and Ti, was characterized by dissolving in $N_2$-sparged 5 M HCl inside the glovebox overnight with shaking. Fe(II) was then determined using the ferrozine method,[54] and total Fe and Ti were determined using inductively coupled plasma mass spectrometry. The specific surface area (multipoint BET SSA) of the titanomagnetite nanoparticles was measured with a Quantachrome Autosorb automated gas sorption system (Quantachrome Co.) using nitrogen gas at 77 K. The samples were dried by degassing at 423 K under vacuum for 24 h before measurements. Particle size and morphology were measured by a JEOL-JEM 2010 transmission electron microscope. TEM samples were prepared by dipping a 400 mesh copper grid coated with lacey carbon film into diluted nanoparticle suspension and then drying it inside the glovebox. Samples were taken out of the glovebox directly before measurements.

**Purification of MtoA.** The details of protein purification and characterization of MtoA were described in Liu et al.[21] Multiple batches of MtoA were prepared. After purification, all purified MtoAs were adjusted to 8 $\mu$M. The purified MtoA (8 $\mu$M) in 20 mM HEPES (pH 7.6) with 150 mM NaCl was purged with dry $N_2$ gas for more than 1 h and then stored at 4 °C in serum bottles capped with thick rubber stoppers and crimp sealed. Protein concentrations were measured with a bicinchoninic acid protein assay kit from Pierce (Rockford, IL, USA). **Wet Chemical Experiments.** All glassware and plastic bottles for wet chemical experiments were soaked in 1% $HNO_3$ overnight and then rinsed several times with distilled and deionized water before use. All chemicals, plastic syringes, tubes, vials, pipet tips, and syringe filters were deoxygenated for at least 24 h inside the glovebox prior to use. All spectroscopic and stopped-flow kinetic measurements as well as batch reactions (including Fe(II) release, MtoA sorption, and reduction experiments) were conducted in the glovebox. DDW was stored in an anoxic chamber for preparation of all solutions and suspensions. All chemicals were reagent grade or better. All experiments were performed in triplicate.

**Fe(II)(aq) Release Experiments.** The equilibrated Fe(II)(aq) concentration released from titanomagnetite nanoparticles in Tris buffer solution (20 mM, with 150 mM NaCl) at pHs 7.3, 8, and 9 was measured. The pH value of the Tris buffer solution was adjusted using 5 N HCl solution. Fe(II)(aq) release experiments were conducted by spiking a known amount of nanoparticle suspension into the buffer solution at a desired pH, to give a concentration of 108 ± 4 $\mu$M Fe(II) equivalents within $Fe_{3-x}Ti_xO_4$, in 1.5 mL centrifuge tubes. The tubes were sealed and continuously shaken for 24 h to allow Fe(II) release from nanoparticles to reach equilibrium. Nanoparticles were then separated from solution by centrifugation for 5 min at 30 000 rpm. The Fe(II) concentration in the supernatant was analyzed by ferrozine assay.

**MtoA Sorption Experiments.** The MtoA sorption experiments were performed to determine the equilibrium distribution of MtoA between in solution and on nanoparticles. Theoretically, the percentage of sorbed MtoA can be measured by using the decrease of UV−vis absorbance of protein. However, purified MtoA was in the oxidized form. Addition of purified MtoA to nanoparticle suspensions can result in reduction and adsorption simultaneously, and the observed absorption spectrum shows the total effect of these two reactions. Therefore, fully reduced MtoA was used as a surrogate of purified MtoA in order to rule out any effect of reduction. It is assumed that the reduced and oxidized MtoA have similar absorption behavior on the surface of the nanoparticles, based on previous observations of a functionally and compositionally similar 10-heme cytochrome OmcA in which the oxidation state switch only caused small rearrangement of heme groups but no significant change in conformation or arrangement of polypeptide.[55] MtoA was fully reduced in the glovebox directly before sorption experiments by gradually adding 10 mM sodium dithionite solution to 0.5 mL of protein stock solution until no changes in the UV−vis spectra were observed. The UV−vis absorption spectra were collected using an Agilent 8452 diode array spectrophotometer (Santa Clara, CA, USA) inside the glovebox. In sorption experiments, known volumes of $Fe_{3-x}Ti_xO_4$ nanoparticle suspension and reduced MtoA were added to the Tris buffer solution mentioned above at the desired pH. The nanoparticle concentration was fixed to give a concentration of 108 ± 4 $\mu$M Fe(II) equivalents within $Fe_{3-x}Ti_xO_4$, and the MtoA concentration was ~8 $\mu$M. The mixture was continuously shaken for 5 min to allow the completion of sorption. The nanoparticles were magnetically separated from solution, and the absorption spectrum of MtoA in solution was measured. The sorbed concentration was calculated by the change of absorbance at 552 or 418 nm.

**MtoA Oxidation of $Fe_{3-x}Ti_xO_4$ Nanoparticles.** The kinetics of nanoparticle oxidation by MtoA was investigated using a Biologic SFM400 stopped-flow system fiber-optically coupled with a BioLogic MOS 250 spectrometer (Knoxville, TN, USA) inside the glovebox. The method was described in detail by Wang et al.[56] Briefly, purified MtoA solution and as-synthesized nanoparticle suspension were diluted in Tris buffer to the desired pH. Known volumes of the

protein solution and nanoparticle suspension were rapidly mixed, and the absorbance at 552 nm was tracked as a function of time. After baseline correction, the Beer–Lambert law can be used to calculate the concentration of oxidized MtoA at time $t$ ($C_t$) from the measured absorbance ($A_t$):

$$C_t = \frac{A_t - C_0\varepsilon_{ox}}{\varepsilon_{ox} - \varepsilon_{red}} \quad (4)$$

where $C_0$ is the initial concentration of oxidized MtoA and $\varepsilon_{ox}$ and $\varepsilon_{red}$ are the molar absorption coefficients of the oxidized and reduced MtoA, respectively.[56] All stopped-flow kinetic experiments were conducted in Tris buffer by mixing 0.8 $\mu$M protein and $Fe_{3-x}Ti_xO_4$ nanoparticles with a concentration of 108 ± 4 $\mu$M Fe(II) equivalents.

The extent of $Fe_{3-x}Ti_xO_4$ oxidation by MtoA was studied by spiking a certain volume of as-synthesized $Fe_{3-x}Ti_xO_4$ nanoparticle suspension into the 0.8 $\mu$M MtoA solution buffered by the Tris solution at the required pH value. The reaction was conducted in a quartz cuvette with a screw cap (Precision Cells Inc.). The cuvette was shaken for 5 min to allow the reactions to reach equilibrium and then put onto a magnate plate for another 5 min to precipitate $Fe_{3-x}Ti_xO_4$ nanoparticles. The supernatant was then moved to a clean cuvette using a pipet for measurement of the UV–vis absorption spectrum. Electron transfer in Fe(II) oxidation by MtoA was measured using the reaction between a suspension of $x$ = 0.38 nanoparticles given an Fe(II) concentration of 108 $\mu$M and 8 $\mu$M of oxidized MtoA solution at pH 7.6. After reaction, the nanoparticles were magnetically separated, and the amount of reduced MtoA was measured using the absorbance at the 552 nm band in the absorption spectrum. The change in Fe(II) concentration in the solid was determined from the cell parameter as described in Pearce et al.[32] by measuring the nanoparticle suspension before and after reaction with MtoA using $\mu$-XRD.

**Analysis of Kinetic Data.** Titanomagnetite oxidation produces titanomaghemite through a topotactic reaction that maintains the inverse spinel structure. The generalized formula for these phases may be written as follows:[33]

$$Fe^{3+}_{2-2x+2/3y}Fe^{2+}_{1+x-y}Ti^{4+}_{x}\square_{y/3}O^{2-}_{4} \quad (5)$$

where $y$ is the oxidation parameter that varies from $0 \le y \le 1$, where $y$ = 0 equates to unoxidized and $y$ = 1 equates to oxidized, with a limit of one electron removed per formula unit. Previous work[21] has shown that all 10 hemes in MtoA participate in electron transfer; thus, the overall reaction between purified MtoA and $Fe_{3-x}Ti_xO_4$ nanoparticles, to produce fully reduce MtoA and fully oxidized titanomaghemite can be expressed as follows:

$$\text{Fe(III)–MtoA} + 10Fe^{3+}_{2-2x}Fe^{2+}_{1+x}Ti^{4+}_{x}O^{2-}_{4} \rightarrow \text{Fe(II)–MtoA} + 10Fe^{3+}_{2-2x+0.667}Fe^{2+}_{1+x-1}Ti^{4+}_{x}\square_{1/3}O^{2-}_{4} \quad (6)$$

The rate law of this reaction can be mathematically expressed as follows:

$$\frac{dC}{dt} = -kCA(1 - (Q/K_{eq})^n) \quad (7)$$

where $k$ is the second-order rate constant, $A$ is the initial concentration of Fe(II) in the $Fe_{3-x}Ti_xO_4$ nanoparticles, $C$ is the initial concentration of purified MtoA, $Q$ is the ion activity product of the redox reaction, $K_{eq}$ is the conditional equilibrium constant, and $n$ is the reaction nonlinearity order. The concentration of oxidized MtoA ($C$) was calculated from the measured absorbance in the stopped-flow system according to eq 4 and plotted against time. The residual Fe(II) concentration was calculated from the electron balance between the reacted Fe(II) and reduced MtoA. The calculated MtoA and Fe(II) concentrations as a function of time were then used to estimate rate parameters in eq 7. The second-order rate constant, the conditional equilibrium constant, and the nonlinearity order were estimated by minimizing the error between calculated and measured concentrations of oxidized MtoA. The values of the square of the correlation coefficient, $R^2$, were greater than 0.95 in all data fits.

**Micro-X-ray Diffraction.** $Fe_{3-x}Ti_xO_4$ nanoparticle suspensions, before and after reaction with MtoA, were characterized in situ by $\mu$-XRD using a Rigaku D/Max Rapid II instrument with a MicroMax 007HF generator fitted with a rotating Cr anode ($\lambda$ = 2.2897 Å) and a two-dimensional (2D) image plate detector. X-rays were focused on the specimen through a 30 $\mu$m diameter collimator. The suspensions were loaded into boron-rich 0.5 mm o.d. capillary tubes (Charles Supper Company) in the glovebox, and the capillaries were sealed with capillary wax (Charles Supper Company). The capillaries were maintained under anoxic conditions until immediately prior to measurement. 2DP, Rigaku 2D data processing software (Ver. 1.0, Rigaku 2007) was used to integrate the diffraction rings captured by the 2D image plate detector. The analysis of diffraction data was done using JADE 8.5 from Materials Data Inc. and the PDF4+ database from ICSD. The details of data fitting were described in Pearce et al.[32]

**X-ray Magnetic Circular Dichroism.** $Fe_{3-x}Ti_xO_4$ nanoparticle suspensions, before and after reaction with MtoA, were characterized using XMCD, which in our case was based on determining the difference spectrum between XA spectra obtained with circularly polarized X-rays in alternating opposing static applied magnetic fields. XMCD is sensitive to the oxidation state and local structure of magnetically ordered iron cations near solid surfaces.[53,57−59] XA spectra at the Fe and Ti $L_{2,3}$ edges were obtained on beamline 4.0.2 at the Advanced Light Source (ALS), Berkeley, CA, using the octapole resistive magnet end-station.[60] Samples were prepared on-site by drying aliquots of the anoxic nanoparticle suspension onto carbon tape attached to the sample manipulator in an anoxic cabinet. In order to preserve the Fe oxidation state of the $Fe_{3-x}Ti_xO_4$ nanoparticles, no attempt was made to separate them from the protein. XA was monitored in total-electron yield (TEY) detection mode, a configuration that emphasizes the nanoparticle–cytochrome interface. In TEY mode, XA spectra are measured by collecting the drain current from the sample to ground. The absorbed photons create core holes that are filled by Auger electron emission. The primary Auger electrons cause a low energy cascade through inelastic scattering processes on the way to the sample surface. The total number of emitted electrons is directly proportional to the probability of the Auger electron creation, that is the absorption probability. For magnetite thin films, it was shown that 67% of the signal comes from the depth interval 0–50 Å, the so-called effective probing depth,[51] a depth equivalent to roughly half the diameter of our nanoparticles. However, given the exponential signal decay into the nanoparticles and given that in a film of nanoparticles of similar or smaller size than the probing depth surface sampling can be geometrically compounded, it is reasonable to assume that the XA/XMCD spectra report primarily just on the upper few angstroms of the nanoparticle surfaces. At each energy point, XA spectra were measured for two opposite applied field directions of 0.6 T. After normalization to the incident beam intensity, the XMCD spectrum is obtained as the difference between the two XA spectra.[61] To obtain the cation distribution over the two structural Fe site types, an XMCD spectrum was fit by means of a nonlinear least-squares analysis, using the calculated spectra for each site. In these calculations, described in van der Laan and Kirkman[52] and van der Laan and Thole,[53] the 10 Dq crystal field parameters were taken as 1.2 and 0.6 eV for Fe $O_h$ and $T_d$ sites. The results were convoluted by a Lorentzian of $C$ = 0.3 (0.5) eV for the $L_3$ ($L_2$) edge to account for intrinsic core–hole lifetime broadening and by a Gaussian of $r$ = 0.2 eV to account for instrumental broadening. The Ti $L_{2,3}$ XAS was also recorded on beamline 4.0.2 at the ALS and is not sensitive to the magnetic field.

## AUTHOR INFORMATION


### Corresponding Author

juan.liu@pnnl.gov


### Notes

The authors declare no competing financial interest.

## ■ ACKNOWLEDGMENTS

This work was funded by PNNL Science Focus Area (SFA), Subsurface Biogeochemical Research (SBR) program, and U.S. Department of Energy (DOE). $\mu$-XRD analyses were performed in the Environmental Molecular Science Laboratory (EMSL), a national user facility supported by the DOE Office of Biological and Environmental Research (OBER) and located at PNNL. XA and XMCD measurements were performed at the Advance Light Source (ALS) supported by the DOE Office of Science, Office of Basic Energy Sciences under contract no. DE-AC02-05CH11231. We gratefully acknowledge the assistance of R.A.D. Pattrick with some of the XA/XMCD measurements at the ALS.

## ■ REFERENCES

(1) Shemetov, A. A.; Nabiev, I.; Sukhanova, A. *ACS Nano* **2012**, *6*, 4585.
(2) Lowry, G. V.; Gregory, K. B.; Apte, S. C.; Lead, J. R. *Environ. Sci. Technol.* **2012**, *46*, 6893.
(3) Moreau, J. W.; Weber, P. K.; Martin, M. C.; Gilbert, B.; Hutcheon, I. D.; Banfield, J. F. *Science* **2007**, *316*, 1600.
(4) Klaine, S. J.; Alvarez, P. J. J.; Batley, G. E.; Fernandes, T. F.; Handy, R. D.; Lyon, D. Y.; Mahendra, S.; McLaughlin, M. J.; Lead, J. R. *Environ. Toxicol. Chem.* **2008**, *27*, 1825.
(5) Sivula, K.; Le Formal, F.; Gratzel, M. *ChemSusChem* **2011**, *4*, 432.
(6) Glasscock, J. A.; Barnes, P. R. F.; Plumb, I. C.; Savvides, N. *J. Phys. Chem. C* **2007**, *111*, 16477.
(7) Thomas, C. R.; Ferris, D. P.; Lee, J. H.; Choi, E.; Cho, M. H.; Kim, E. S.; Stoddart, J. F.; Shin, J. S.; Cheon, J.; Zink, J. I. *J. Am. Chem. Soc.* **2010**, *132*, 10623.
(8) Gupta, A. K.; Gupta, M. *Biomaterials* **2005**, *26*, 3995.
(9) Stanley, S. A.; Gagner, J. E.; Damanpour, S.; Yoshida, M.; Dordick, J. S.; Friedman, J. M. *Science* **2012**, *336*, 604.
(10) Ju-Nam, Y.; Lead, J. R. *Sci. Total Environ.* **2008**, *400*, 396.
(11) Smith, J. N.; Klein, J.; Minard, K.; Hostetler, K.; Pearce, C.; Pounds, J. In Society of Toxicology Conference Annual Meeting, San Francisco, CA, March 11−15, 2012; Society of Toxicology: Reston, VA.
(12) Hochella, M. F.; Lower, S. K.; Maurice, P. A.; Penn, R. L.; Sahai, N.; Sparks, D. L.; Twining, B. S. *Science* **2008**, *319*, 1631.
(13) Wigginton, N. S.; Haus, K. L.; Hochella, M. F. *J. Environ. Monit.* **2007**, *9*, 1306.
(14) Pan, Y.; Du, X. W.; Zhao, F.; Xu, B. *Chem. Soc. Rev.* **2012**, *41*, 2912.
(15) Miot, J.; Benzerara, K.; Morin, G.; Kappler, A.; Bernard, S.; Obst, M.; Ferard, C.; Skouri-Panet, F.; Guigner, J. M.; Posth, N.; Galvez, M.; Brown, G. E.; Guyot, F. *Geochim. Cosmochim. Acta* **2009**, *73*, 696.
(16) Emerson, D.; Fleming, E. J.; McBeth, J. M. *Annu. Rev. Microbiol.* **2010**, *64*, 561.
(17) Konhauser, K. O.; Kappler, A.; Roden, E. E. *Elements* **2011**, *7*, 89.
(18) Emerson, D.; Moyer, C. *Appl. Environ. Microbiol.* **1997**, *63*, 4784.
(19) Emerson, D.; Rentz, J. A.; Lilburn, T. G.; Davis, R. E.; Aldrich, H.; Chan, C.; Moyer, C. L. *PLoS One* **2007**, *2*, e667.
(20) Shi, L.; Rosso, K. M.; Zachara, J. M.; Fredrickson, J. K. *Biochem. Soc. Trans.* **2012**, *40*, 1261.
(21) Liu, J.; Wang, Z.; Belchik, S. M.; Edwards, M. J.; Liu, C.; Kennedy, D. W.; Merkley, E. D.; Lipton, M. S.; Butt, J. N.; Richardson, D. J.; Zachara, J. M.; Fredrickson, J. K.; Rosso, K. M.; Shi, L. *Front. Microbiol.* **2012**, *3*, 37.
(22) Weber, K. A.; Picardal, F. W.; Roden, E. E. *Environ. Sci. Technol.* **2001**, *35*, 1644.
(23) Hansel, C. M.; Benner, S. G.; Neiss, J.; Dohnalkova, A.; Kukkadapu, R. K.; Fendorf, S. *Geochim. Cosmochim. Acta* **2003**, *67*, 2977.
(24) Cornell, R. M.; Schwertmann, U. *The Iron Oxides: Structure, Properties, Reactions, Occurrences and Uses*, 2nd ed.; Wiley-VCH: Weinheim, Germany, 2003.
(25) Pearce, C. I.; Henderson, C. M. B.; Pattrick, R. A. D.; van der Laan, G.; Vaughan, D. J. *Am. Mineral.* **2006**, *91*, 880.
(26) Baer, D. R.; Grosz, A. E.; Ilton, E. S.; Krupka, K. M.; Liu, J.; Penn, R. L.; Pepin, A. *Phys. Chem. Earth* **2010**, *35*, 233.
(27) Pearce, C. I.; Liu, J.; Baer, D. R.; Qafoku, O.; Heald, S. M.; Arenholz, E.; Grosz, A. E.; McKinley, J. P.; Resch, C. T.; Bowden, M. E.; Engelhard, M. H.; Rosso, K. M. *Geochim. Cosmochim. Acta* **2013**, accepted for publication.
(28) Pankhurst, Q. A.; Connolly, J.; Jones, S. K.; Dobson, J. *J. Phys. D: Appl. Phys.* **2003**, *36*, R167.
(29) Mornet, S.; Vasseur, S.; Grasset, F.; Duguet, E. *J. Mater. Chem.* **2004**, *14*, 2161.
(30) Lee, J. H.; Jang, J. T.; Choi, J. S.; Moon, S. H.; Noh, S. H.; Kim, J. W.; Kim, J. G.; Kim, I. S.; Park, K. I.; Cheon, J. *Nat. Nanotechnol.* **2011**, *6*, 418.
(31) Mahmoudi, M.; Lynch, I.; Ejtehadi, M. R.; Monopoli, M. P.; Bombelli, F. B.; Laurent, S. *Chem. Rev.* **2011**, *111*, 5610.
(32) Pearce, C. I.; Qafoku, O.; Liu, J.; Arenholz, E.; Heald, S. M.; Kukkadapu, R. K.; Gorski, C. A.; Henderson, C. M. B.; Rosso, K. M. *J. Colloid Interface Sci.* **2012**, *387*, 24.
(33) Worm, H. U.; Banerjee, S. K. *Geophys. Res. Lett.* **1984**, *11*, 169.
(34) Tronc, E.; Jolivet, J. P.; Belleville, P.; Livage, J. *Hyperfine Interact.* **1989**, *46*, 637.
(35) Jolivet, J. P.; Tronc, E. *J. Colloid Interface Sci.* **1988**, *125*, 688.
(36) Sedlak, D. L.; Chan, P. G. *Geochim. Cosmochim. Acta* **1997**, *61*, 2185.
(37) Wehrli, B. In *Aquatic Chemcial Kinetics: Reaction Rates of Processes in Natural Waters*; Stumm, W., Ed.; Wiley: New York, 1990; p 311.
(38) Liu, J.; Pearce, C. I.; Qafoku, O.; Arenholz, E.; Heald, S. M.; Rosso, K. M. *Geochim. Cosmochim. Acta* **2012**, *92*, 67.
(39) Liger, E.; Charlet, L.; Van Cappellen, P. *Geochim. Cosmochim. Acta* **1999**, *63*, 2939.
(40) Stumm, W.; Sulzberger, B. *Geochim. Cosmochim. Acta* **1992**, *56*, 3233.
(41) Sun, Z. X.; Su, F. W.; Forsling, W.; Samskog, P. O. *J. Colloid Interface Sci.* **1998**, *197*, 151.
(42) Pang, S. C.; Chin, S. F.; Anderson, M. A. *J. Colloid Interface Sci.* **2007**, *311*, 94.
(43) Gorski, C. A.; Scherer, M. M. *Am. Mineral.* **2010**, *95*, 1017.
(44) Neumann, A.; Hofstetter, T. B.; Skarpeli-Liati, M.; Schwarzenbach, R. P. *Environ. Sci. Technol.* **2009**, *43*, 4082.
(45) Neumann, A.; Hofstetter, T. B.; Lussi, M.; Cirpka, O. A.; Petit, S.; Schwarzenbach, R. P. *Environ. Sci. Technol.* **2008**, *42*, 8381.
(46) Felmy, A. R.; Moore, D. A.; Rosso, K. M.; Qafoku, O.; Rai, D.; Buck, E. C.; Ilton, E. S. *Environ. Sci. Technol.* **2011**, *45*, 3952.
(47) Peterson, M. L.; Brown, G. E.; Parks, G. A. *Colloids Surf., A* **1996**, *107*, 77.
(48) Latta, D. E.; Gorski, C. A.; Boyanov, M. I.; O'Loughlin, E. J.; Kemner, K. M.; Scherer, M. M. *Environ. Sci. Technol.* **2012**, *46*, 778.
(49) Lilova, K. I.; Pearce, C. I.; Gorski, C.; Rosso, K. M.; Navrotsky, A. *Am. Mineral.* **2012**, *97*, 1330.
(50) Marcus, R. A.; Sutin, N. *Biochim. Biophys. Acta* **1985**, *811*, 265.
(51) Gota, S.; Gautier-Soyer, M.; Sacchi, M. *Phys. Rev. B* **2000**, *62*, 4187.
(52) van der Laan, G.; Kirkman, I. W. *J. Phys.: Condens. Matter* **1992**, *4*, 4189.
(53) van der Laan, G.; Thole, B. T. *Phys. Rev. B* **1991**, *43*, 13401.
(54) Stookey, L. L. *Anal. Chem.* **1970**, *42*, 779.
(55) Johs, A.; Shi, L.; Droubay, T.; Ankner, J. F.; Liang, L. *Biophys. J.* **2010**, *98*, 3035.
(56) Wang, Z. M.; Liu, C. X.; Wang, X. L.; Marshall, M. J.; Zachara, J. M.; Rosso, K. M.; Dupuis, M.; Fredrickson, J. K.; Heald, S.; Shi, L. *Appl. Environ. Microbiol.* **2008**, *74*, 6746.

(57) Chen, C. T.; Idzerda, Y. U.; Lin, H. J.; Smith, N. V.; Meigs, G.; Chaban, E.; Ho, G. H.; Pellegrin, E.; Sette, F. *Phys. Rev. Lett.* **1995**, *75*, 152.
(58) Stohr, J. *J. Electron Spectrosc. Relat. Phenom.* **1995**, *75*, 253.
(59) van der Laan, G.; Zaanen, J.; Sawatzky, G. A.; Karnatak, R.; Esteva, J. M. *Phys. Rev. B* **1986**, *33*, 4253.
(60) Arenholz, E.; Prestemon, S. O. *Rev. Sci. Instrum.* **2005**, *76*, 083908.
(61) Pattrick, R. A. D.; Van der Laan, G.; Henderson, C. M. B.; Kuiper, P.; Dudzik, E.; Vaughan, D. J. *Eur. J. Mineral.* **2002**, *14*, 1095.